Reduced dynamical models of nonisothermal transitional grooved-channel flow

R. A. Sahan, A. Liakopoulos,[a] and H. Gunes
Department of Mechanical Engineering and Mechanics, Lehigh University, Bethlehem, Pennsylvania 18015-3085

(Received 16 July 1996; accepted 31 October 1996)

Reduced dynamical models are derived for transitional flow and heat transfer in a periodically grooved channel. The full governing partial differential equations are solved by a spectral element method. Spontaneously oscillatory solutions are computed for Reynolds number $Re \geqslant 300$ and proper orthogonal decomposition is used to extract the empirical eigenfunctions at $Re=430$, 750, 1050, and $Pr=0.71$. In each case, the organized spatio-temporal structures of the thermofluid system are identified, and their dependence on Reynolds number is discussed. Low-dimensional models are obtained for $Re=430$, 750, and 1050 using the computed empirical eigenfunctions as basis functions and applying Galerkin's method. At least four eigenmodes for each field variable are required to predict stable, self-sustained oscillations of correct amplitude at ''design'' conditions. Retaining more than six eigenmodes may reduce the accuracy of the low-order models due to noise introduced by the low-energy high order eigenmodes. The low-order models successfully describe the dynamical characteristics of the flow for Re close to the design conditions. Far from the design conditions, the reduced models predict quasi-periodic or period-doubling routes to chaos as Re is increased. The case $Pr=7.1$ is briefly discussed. [S1070-6631(97)00303-6]

I. INTRODUCTION

There is evidence that certain thermofluid systems exhibit chaotic behavior through the nonlinear interaction of a small number of degrees of freedom and that the early stages of the transition process can be identified in phase space by low-dimensional dynamical behavior. This observation provides the basis for the construction of low-order models (LOMs) describing the dynamics of transitional flows. Low-order models replace the system of governing partial differential equations (PDEs, infinite-dimensional systems) with a relatively small set of ordinary differential equations (ODEs, finite-dimensional systems). Low-dimensional dynamical models have been reported for the description of coherent structures in the wall region of a turbulent boundary layer,[1] Rayleigh–Benard convection,[2] isothermal grooved channel flow and flow past a cylinder,[3] transitional flat-plate boundary layer,[4] free convection in vertical channels,[5,6] and heat transfer by forced convection in a periodically grooved channel.[7,8]

PDEs can be transformed into systems of ODEs by well-known procedures, e.g., the method of weighted residuals. This approach has been successfully applied using a variety of basis functions, e.g., trigonometric functions, orthogonal polynomials,[9] or spline functions.[10,11] In general, these methods lead to large systems of ODEs. Low-dimensional dynamical models may be developed by expanding the unknown functions in terms of basis functions that are constructed for each system separately and reflect the behavior of the system in the vicinity of some values of the controlling parameters. A rigorous methodology for obtaining a set of optimal basis functions is the Proper Orthogonal Decomposition (POD), or method of empirical eigenfunctions, first introduced in fluid mechanics by Lumley[12] as a tool for the extraction of coherent structures in turbulent flows. The snapshot version of POD[13] provides an efficient way of extracting the empirical eigenfunctions of large data sets. POD identifies the most energetic eigenmodes and enables us to compress numerical or experimental data by retaining a small number of such modes. These modes store the information necessary for accurate dynamical decomposition of time-varying fields and, when appropriately combined, they systematically identify the dynamical (spatio-temporal) coherent structures. A large number of POD applications for analysis and postprocessing of experimental data has been reported, e.g., Glauser and George,[14] Lu and Smith,[15] and Bonnet and Glauser.[16] For an overview of POD and its applications, see Sirovich[17] and Berkooz *et al.*[18]

The stability and heat transfer characteristics of flow in a

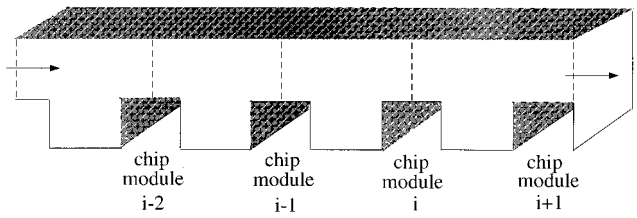

FIG. 1. Grooved channel configuration.

[a]Corresponding author. Telephone: (610) 758-4929; Fax: (610) 758-6224; Electronic mail: al03@lehigh.edu

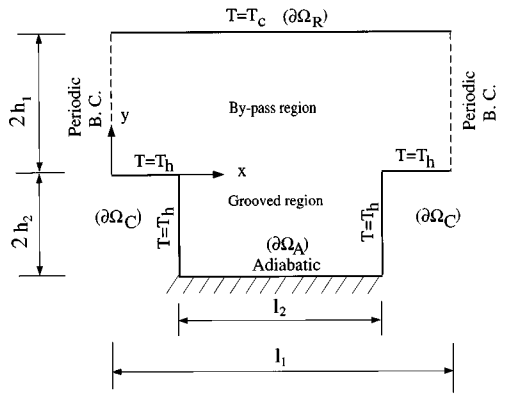

FIG. 2. Computational domain and boundary conditions. $h_2/h_1=0.75$, $l_1/h_1=5.0$, $l_2/h_1=3.0$.

grooved channel have been studied by many researchers.[19–22] The configuration involves sharp corners leading to flow separation and temporal hydrodynamic instabilities even at low or moderate values of Reynolds number (Re). The flow is time independent when $\mathrm{Re}<\mathrm{Re}_c$, and exhibits self-sustained oscillations for $\mathrm{Re}\geqslant\mathrm{Re}_c$, where Re_c denotes the critical Reynolds number at the onset of temporal instability. The isothermal case has been analyzed using POD by Deane *et al.*[3] and Sahan *et al.*[7] Sahan *et al.*[8] included temperature effects and developed low-order models of the thermofluid system at slightly supercritical conditions (Re=430).

In this paper, the snapshot version of proper orthogonal decomposition has been applied to transitional flow and heat transfer in the grooved channel shown in Fig. 1. This configuration is an idealization of channel geometries that appear frequently in cooling of electronic equipment where the protrusions are formed by chip modules. The channel geometry is assumed to be periodic and entrance effects are ignored. POD is performed at Pr=0.71 and Re=430, 750, and 1050. The case Pr=7.1 and Re=430 is briefly discussed in Sec. V. At these values of Re the flow is time periodic. For each Reynolds number, a low-dimensional set of nonlinear ODEs is derived by using Galerkin projection. The ability of the reduced models to describe the dynamics of the flow and temperature fields is examined.

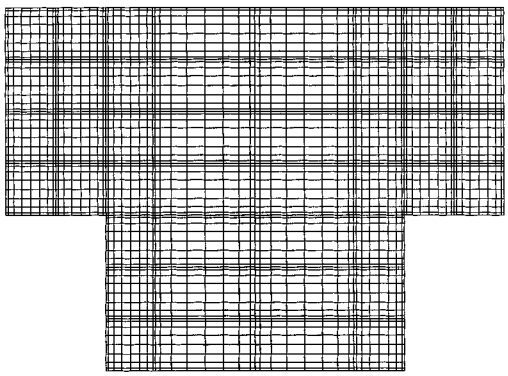

FIG. 3. Computational mesh. 44 spectral elements each with 9×9 collocation points.

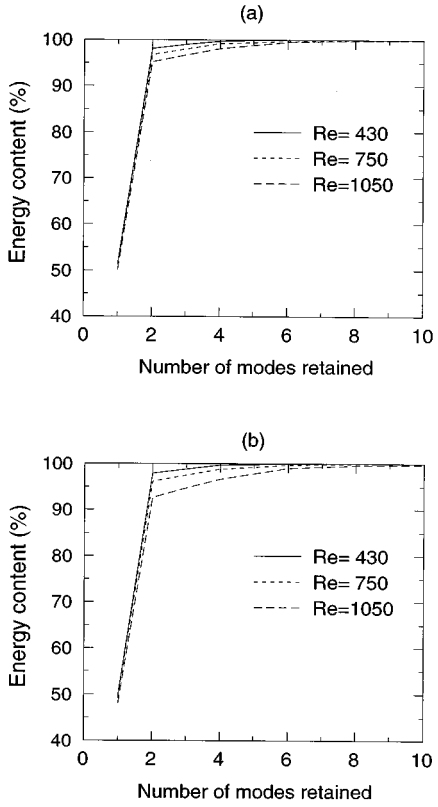

FIG. 4. Contribution of eigenvalues to the total flow and temperature fluctuation energy. (a) Velocity modes, (b) temperature modes, Pr=0.71.

II. FULL MODEL: FORMULATION AND SOLUTION METHOD

Figure 1 shows the grooved channel configuration under study. The velocity field is assumed to be incompressible and periodically fully developed.[22] Neglecting buoyancy, viscous dissipation, and energy generation, the partial differential equations governing constant-property, time-dependent flow, and heat transfer can be written in dimensionless form as follows:

Conservation of mass:

$$\nabla\cdot\mathbf{V}=0, \tag{1}$$

Conservation of momentum:

$$\frac{\partial\mathbf{V}}{\partial t}+(\mathbf{V}\cdot\nabla)\mathbf{V}=-\nabla P+\frac{1}{\mathrm{Re}}\nabla^2\mathbf{V}+\mathbf{F}, \tag{2}$$

Conservation of energy:

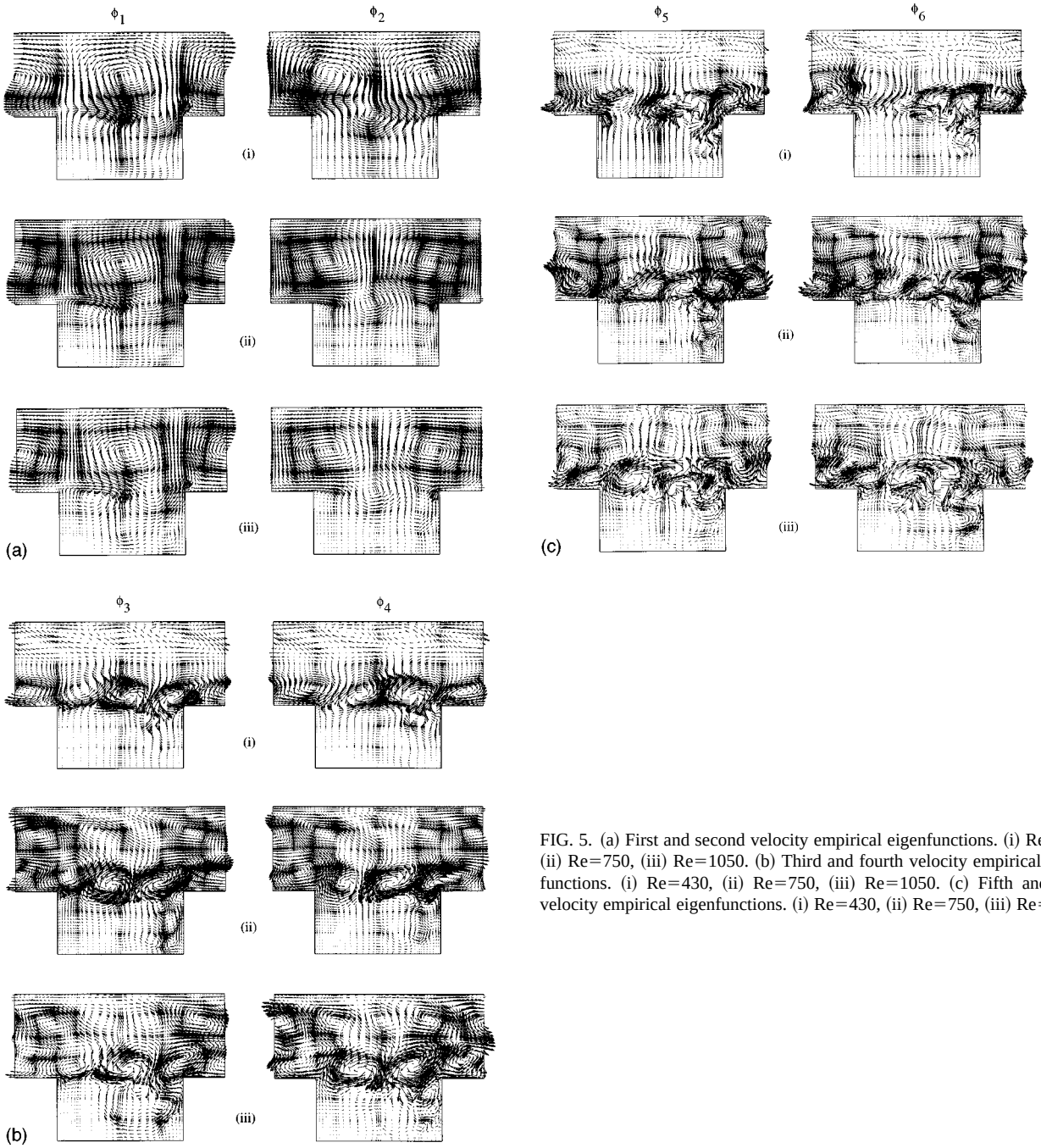

FIG. 5. (a) First and second velocity empirical eigenfunctions. (i) Re=430, (ii) Re=750, (iii) Re=1050. (b) Third and fourth velocity empirical eigenfunctions. (i) Re=430, (ii) Re=750, (iii) Re=1050. (c) Fifth and sixth velocity empirical eigenfunctions. (i) Re=430, (ii) Re=750, (iii) Re=1050.

$$\frac{\partial \Theta}{\partial t} + (\mathbf{V}\cdot\nabla)\Theta = \frac{1}{\mathrm{Re\ Pr}}\nabla^2\Theta. \tag{3}$$

In writing the governing equations in this form, the dimensionless variables have been defined as

$$X=\frac{x}{h_1}, \quad Y=\frac{y}{h_1}, \quad t=\frac{U_{\mathrm{ref}}}{h_1}t^*, \quad U=\frac{u}{U_{\mathrm{ref}}},$$

$$V=\frac{v}{U_{\mathrm{ref}}}, \quad P=\frac{p}{\rho U_{\mathrm{ref}}^2}, \quad \Theta=\frac{T-T_c}{T_h-T_c}, \quad \text{and} \quad \mathbf{F}=\frac{h_1\mathbf{f}}{U_{\mathrm{ref}}^2},$$

where $2h_1$ denotes the width of the bypass part of the channel (see Fig. 2), ρ is the fluid density, p is the static pressure, T denotes the local temperature, and $\mathbf{f}$ denotes all forcing contributions. The dimensionless parameters appearing in Eqs. (2) and (3), the Reynolds number Re, and the Prandtl number Pr, are defined as

$$\mathrm{Re}=\frac{U_{\mathrm{ref}}\,h_1}{\nu}, \quad \mathrm{Pr}=\frac{\nu}{\alpha},$$

TABLE I. The ten largest normalized eigenvalues and their respective contributions to the total flow fluctuation energy.

	Re=430 F_x=0.0053 F_y=0		Re=750 F_x=0.0035 F_y=0		Re=1050 F_x=0.0028 F_y=0	
Modes	Normalized eigenvalue	Cumulative energy, %	Normalized eigenvalue	Cumulative energy, %	Normalized eigenvalue	Cumulative energy, %
1	0.513 95	51.39	0.511 59	51.16	0.500 67	50.07
2	0.467 41	98.14	0.456 23	96.78	0.451 21	95.19
3	0.008 29	98.96	0.012 29	98.01	0.014 99	96.69
4	0.007 67	99.72	0.011 31	99.14	0.014 31	98.12
5	0.001 17	99.84	0.002 93	99.43	0.007 02	98.82
6	0.001 13	99.95	0.002 91	99.73	0.006 67	99.48
7	0.000 16	99.97	0.000 85	99.81	0.001 79	99.67
8	0.000 15	99.99	0.000 73	99.88	0.001 31	99.80
9	0.000 04	99.99	0.000 34	99.91	0.000 65	99.86
10	0.000 03	99.99	0.000 29	99.94	0.000 47	99.91

where ν denotes the kinematic viscosity, α is the fluid thermal diffusivity, and $U_{\text{ref}}=3/2U_{\text{av}}$ where U_{av} is the average velocity at a channel cross section. We consider the flow far from the channel entrance, and taking into account the spatial periodicity of the channel, we solve the governing equations in one computational module by imposing periodic boundary conditions in the streamwise direction (see Fig. 2). The remaining boundary conditions considered in this study are: (i) no slip conditions at the solid–fluid interfaces, (ii) uniform temperature distribution along the top channel wall ($T=T_c=T_{\text{cold}}$) as well as along the protruding surfaces ($T=T_h=T_{\text{hot}}$), and (iii) adiabatic conditions along the bottom wall segment between the protruding modules (see Fig. 2).

Equations (1)–(3) with the corresponding boundary conditions are solved by a spectral element method.[23] Implementation of the numerical method is based on Nekton, a computer program developed by Patera and his co-workers[24] to simulate steady and unsteady incompressible fluid flow, heat, and mass transfer. In our simulations, 44 two-dimensional spectral elements were used (see Fig. 3). Numerical solutions were obtained for order of interpolants, $N=4$, 6, 8, 10, and 12. Increasing N from 8 to 10 or 12 results in no significant changes in the solution. Values of the field variables at representative fixed locations and integrals of the field variables over the entire domain change by less than 0.6%. Results are presented for $h_2/h_1=0.75$, $l_1/h_1=5.0$, $l_2/h_1=3.0$ (see Fig. 2). For these parameters, spontaneous self-sustained oscillations appear at $\text{Re}_c\simeq 300$.

III. DEVELOPMENT OF LOW ORDER MODELS

The time-dependent data obtained by direct numerical simulation at a supercritical Reynolds number ($\text{Re}>\text{Re}_c$) are first decomposed into time-averaged ($\mathbf{V},\Theta$) and time-varying ($\mathbf{V}',\Theta'$) parts:

$$\mathbf{V}(\mathbf{X},t)=\overline{\mathbf{V}}(\mathbf{X})+\mathbf{V}'(\mathbf{X},t),$$
$$\Theta(\mathbf{X},t)=\overline{\Theta}(\mathbf{X})+\Theta'(\mathbf{X},t). \tag{4}$$

Then, the empirical eigenfunctions are constructed by linearly combining the time-varying parts of the field variables,[13]

TABLE II. The ten largest normalized eigenvalues and their respective contributions to the total temperature fluctuation ''energy'' (Pr=0.71).

	Re=430		Re=750		Re=1050	
Modes	Normalized eigenvalue	Cumulative energy, %	Normalized eigenvalue	Cumulative energy, %	Normalized eigenvalue	Cumulative energy, %
1	0.497 70	49.77	0.491 61	49.16	0.474 87	47.49
2	0.481 20	97.89	0.469 38	96.10	0.451 76	92.67
3	0.008 88	98.78	0.013 71	97.47	0.019 92	94.66
4	0.008 57	99.64	0.013 07	98.77	0.019 09	96.56
5	0.001 58	99.79	0.004 46	99.22	0.012 51	97.81
6	0.001 53	99.94	0.004 27	99.65	0.012 09	99.02
7	0.000 21	99.97	0.001 07	99.75	0.002 75	99.30
8	0.000 20	99.99	0.001 03	99.86	0.002 60	99.56
9	0.000 03	99.99	0.000 43	99.90	0.001 33	99.69
10	0.000 03	99.99	0.000 40	99.94	0.001 07	99.80

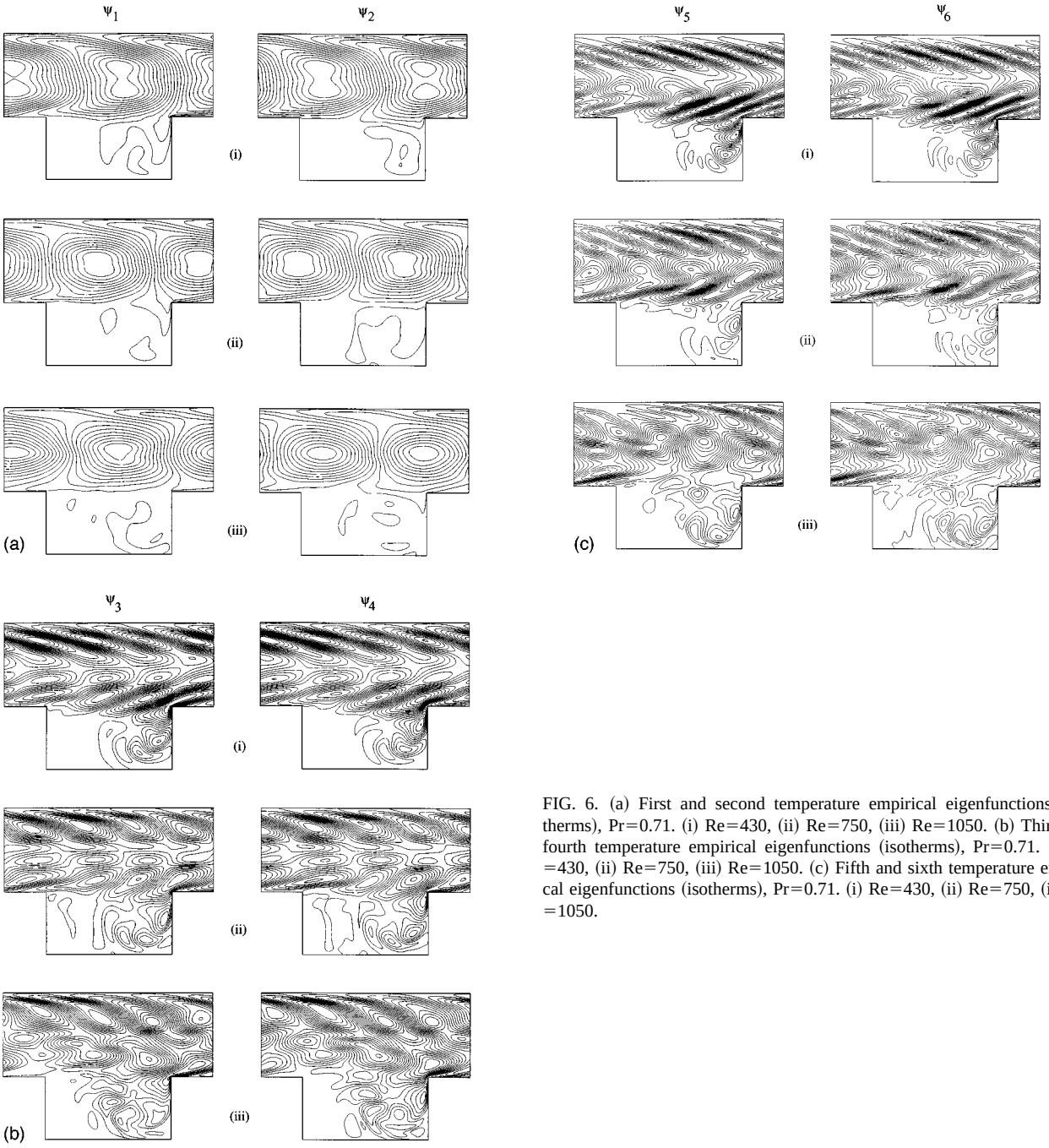

FIG. 6. (a) First and second temperature empirical eigenfunctions (isotherms), Pr=0.71. (i) Re=430, (ii) Re=750, (iii) Re=1050. (b) Third and fourth temperature empirical eigenfunctions (isotherms), Pr=0.71. (i) Re =430, (ii) Re=750, (iii) Re=1050. (c) Fifth and sixth temperature empirical eigenfunctions (isotherms), Pr=0.71. (i) Re=430, (ii) Re=750, (iii) Re =1050.

$$\boldsymbol{\phi}_k(\mathbf{X})=\sum_{i=1}^{M}\alpha_{ki}\mathbf{V}_i'(\mathbf{X},t_i),\quad \psi_k(\mathbf{X})=\sum_{i=1}^{M}\beta_{ki}\Theta_i'(\mathbf{X},t_i),\qquad (5)$$

where α_k (β_k) denotes the kth eigenvector of the velocity (temperature) correlation matrix, and M is the number of snapshots. For the velocity field, the elements of the correlation matrix C are given by

$$C_{mn}=\frac{1}{M}\int_{\Omega}\mathbf{V}_m'(\mathbf{X},t_m)\cdot\mathbf{V}_n'(\mathbf{X},t_n)d\Omega,\qquad (6)$$

while for the temperature field

$$C_{mn}=\frac{1}{M}\int_{\Omega}\Theta_m'(\mathbf{X},t_m)\Theta_n'(\mathbf{X},t_n)d\Omega.\qquad (7)$$

The eigenvalues of matrix C and the empirical eigenfunctions, Eq. (5), have the following properties:[13,18]

(a) The eigenvalues λ_m, $m=1,2,\ldots,M$, are real and nonnegative and they are ordered as $\lambda_1\geqslant\lambda_2\geqslant\lambda_3\geqslant\cdots\geqslant\lambda_M\geqslant 0$.

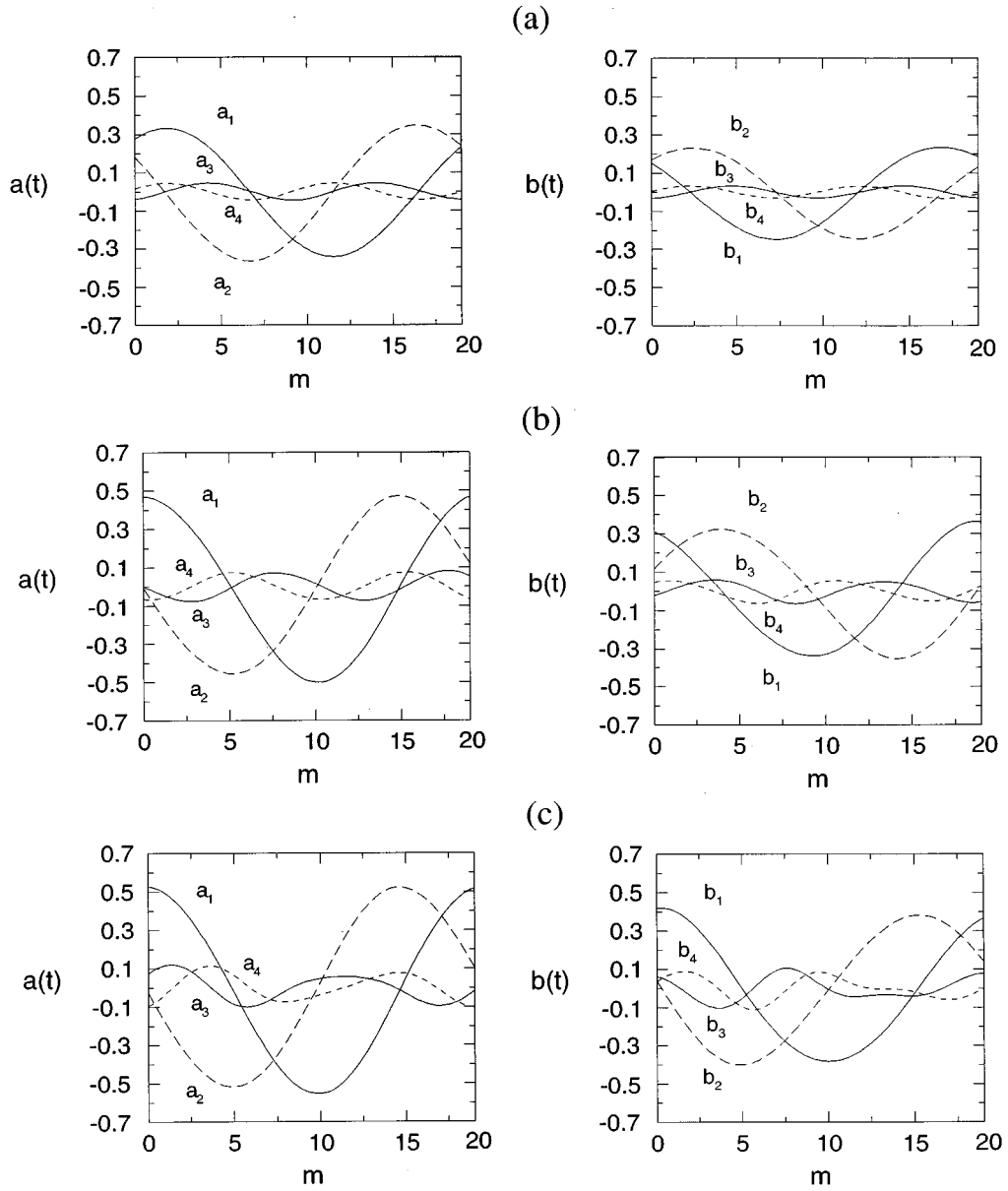

FIG. 7. Temporal expansion coefficients computed by direct projection of snapshots on the eigenfunctions, Pr=0.71. (a) Re=430, (b) Re=750, (c) Re=1050.

(b) Each eigenvalue represents the fluctuation ''energy'' that the corresponding eigenfunction contributes to the flow (temperature) field.

(c) The eigenfunctions are orthogonal to each other and, after normalization, form orthonormal bases,

$$\int_{\Omega} \boldsymbol{\phi}_i \cdot \boldsymbol{\phi}_j d\Omega = \delta_{ij}, \quad \int_{\Omega} \psi_i \psi_j d\Omega = \delta_{ij}. \tag{8}$$

(d) The velocity empirical eigenfunctions are divergence free (since the flow is incompressible).

The time-varying parts of the velocity and temperature fields can be expressed in terms of the normalized eigenfunctions,

$$\begin{aligned} \mathbf{V}'(\mathbf{X},t) &= \sum_{k=1}^{M_1} a_k(t)\,\boldsymbol{\phi}_k(\mathbf{X}), \\ \Theta'(\mathbf{X},t) &= \sum_{k=1}^{M_2} b_k(t)\,\psi_k(\mathbf{X}), \end{aligned} \tag{9}$$

where $\boldsymbol{\phi}_k(\psi_k)$ denotes the kth eigenfunction for the velocity (temperature) field and M_1, M_2 denote the number of modes retained in the expansions. When few modes capture most of the fluctuating ''energy,'' we select $M_1 \ll M$ and $M_2 \ll M$ in order to keep the dimensionality of the reduced model low.

Substituting Eq. (9) into Eqs. (2) and (3), applying Galerkin method, and making use of the orthonormality property of the empirical eigenfunctions, we obtain a system

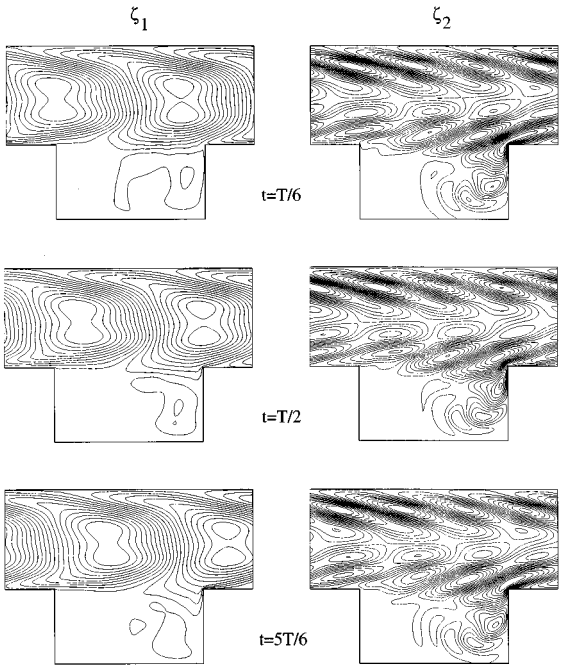

FIG. 8. Reconstructed temperature spatio-temporal structures, Pr=0.71. (a) ζ_1, (b) ζ_2, Re=430, T=period of oscillation.

of nonlinear ODEs for the expansion coefficients $a_k(t)$ and $b_k(t)$:

$$\frac{da_k}{dt} = A_k + \frac{1}{\mathrm{Re}} B_k + C_{ki} a_i + \frac{1}{\mathrm{Re}} D_{ki} a_i + E_{kij} a_i a_j ,$$

$$k = 1,2,\ldots,M_1 , \tag{10}$$

$$\frac{db_k}{dt} = F_k + \frac{1}{\mathrm{Re\ Pr}} G_k + H_{ki} a_i + K_{ki} b_i + \frac{1}{\mathrm{Re\ Pr}} L_{ki} b_i + M_{kij} a_i b_j , \quad k = 1,2,\ldots,M_2 . \tag{11}$$

The coefficients appearing in the above equations are related to the various inner products among the eigenfunctions and/or mean flow and temperature fields. Specific results for these coefficients can be obtained from the authors. The integrals required in POD and in the Galerkin projection have been carried out using Gauss quadrature on the Gauss–Legendre–Lobatto nodes on which the input data are known. Carrying out the required integrations by conventional numerical quadrature methods leads to considerable deviations when low spatial resolution (small N) solutions of the full model are used. Note that Eq. (10) is independent of the temperature field since we consider incompressible flow, constant fluid viscosity, and buoyancy forces are neglected. Note also that expansions (9) satisfy the appropriate boundary conditions and that for periodic boundary conditions there is no contribution of the pressure term in Eq. (10) (see Deane *et al.*[3]).

IV. RESULTS FOR Pr=0.71

A. Eigenvalues

Twenty snapshots ($M=20$), equally spaced over one cycle, were used in the proper orthogonal decomposition. Increasing M has negligible effect on the results. The ten largest eigenvalues and their cumulative contribution to the flow and temperature fluctuation ''energy'' are listed in Tables I and II. The eigenvalues are normalized by requiring $\Sigma\lambda_i=1$ and they are ordered based on their magnitude. For the values of Re considered in this study the eigenvalues occur in pairs. The eigenvalues belonging to a pair have approximately equal magnitude.

For Re=430 the first velocity modal pair (first and second velocity eigenmodes) captures 98.1% of the total flow fluctuation energy. The cumulative contribution of the two most energetic modal pairs is 99.7% while the three most energetic pairs (six largest velocity eigenvalues) contain almost the total flow fluctuation energy [see Table I and Fig. 4(a)]. As Re increases, the percentage of energy contained in the first two modes (the first modal pair) decreases while the relative contribution of the third and fourth modes to the total fluctuation energy increases (see Table I).

Turning to the energy distribution among temperature modes, Table II shows that, as Re increases from 430 to 1050, the contribution of the first and second temperature modes decreases while the third and fourth modes gain share. The drop in the contribution of the first temperature modal pair is significantly higher than the drop in the contribution of the first velocity modal pair (compare Tables I and II). As a consequence, more modes are necessary to capture the same percentage of the temperature fluctuation energy as Re increases. For Re=430, four modes retain 99.6% of the entire fluctuation energy while for Re=750 and Re=1050, the same modes capture only 98.8% and 96.6% of the fluctuation energy, respectively. Note, however, that the first six modes contain more than 99.0% of the fluctuating energy in all three cases [see Table II and Fig. 4(b)].

B. Eigenfunctions

The empirical eigenfunctions $\boldsymbol{\phi}_i$ and ψ_i, $i=1,2,...,6$ are shown in Figs. 5 and 6 for Re=430, 750, and 1050. The two most energetic eigenfunctions ($i=1,2$) contain the large scale features of each field while higher modes (of lower energy level) capture the small scale features of the fields [compare Fig. 5(a) with Figs. 5(b)–5(c) and Fig. 6(a) with Figs. 6(b)–6(c)]. The eigenfunctions occur in pairs, $(\boldsymbol{\phi}_1,\boldsymbol{\phi}_2)$, $(\boldsymbol{\phi}_3,\boldsymbol{\phi}_4),\ldots,(\psi_1,\psi_2),(\psi_3,\psi_4),\cdots$. Within each pair the eigenfunctions are phase shifted by approximately a quarter wavelength in the bypass region of the channel.

At Re=430, large scale features in $(\boldsymbol{\phi}_1,\boldsymbol{\phi}_2)$ cover almost the whole bypass region extending slightly to the groove portion of the channel [Fig. 5(a), case i]. Small scale features

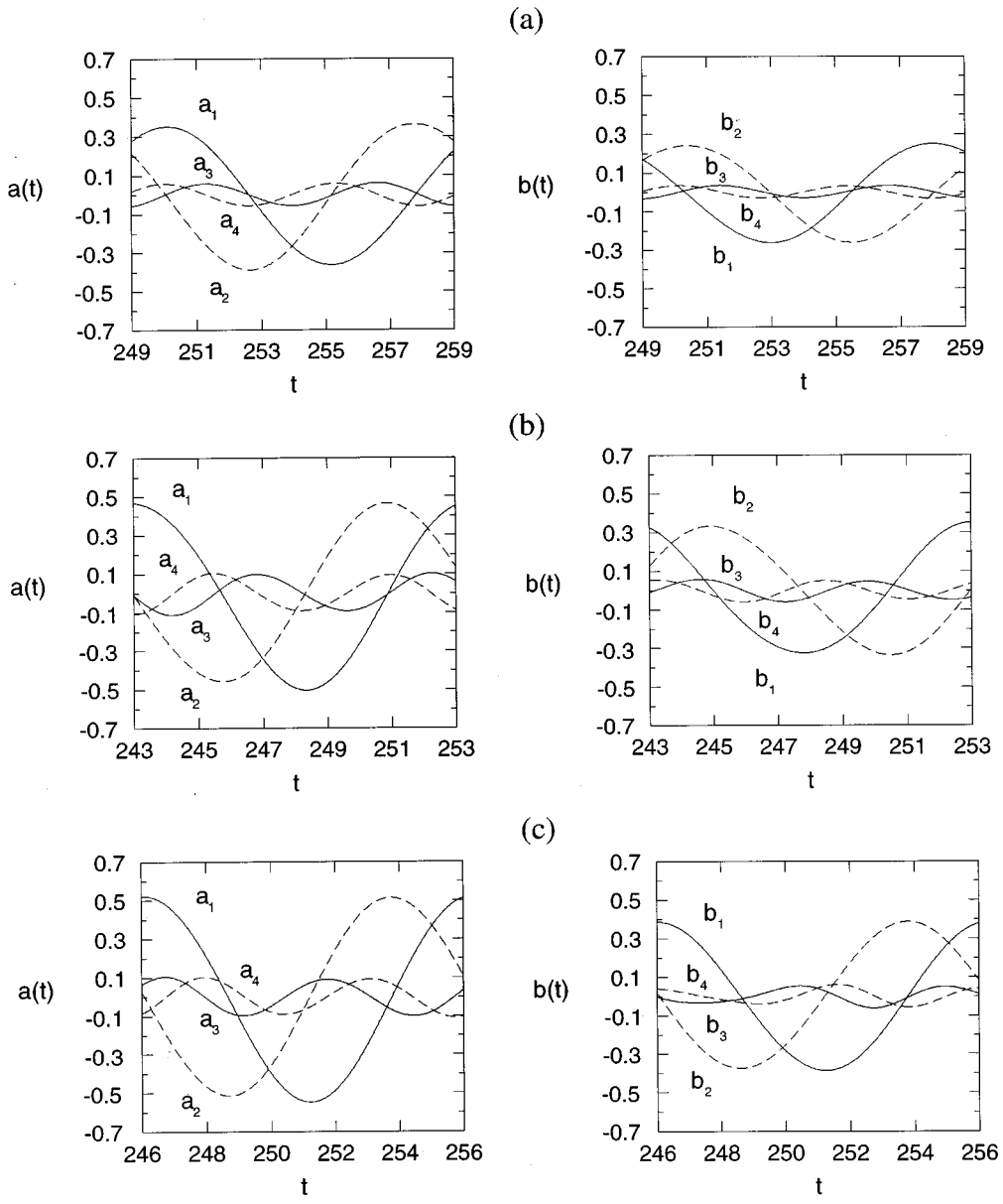

FIG. 9. Temporal expansion coefficients computed by the low-order models at design conditions, $\mathrm{Pr}=\mathrm{Pr}_0=0.71$, $M_1=M_2=4$. (a) $\mathrm{Re}=\mathrm{Re}_0=430$, (b) $\mathrm{Re}=\mathrm{Re}_0=750$, (c) $\mathrm{Re}=\mathrm{Re}_0=1050$.

in the second and third modal pairs are located in the shear layer formed at the intersections of the bypass and grooved regions, and even smaller scale features appear in the upper portion of the bypass region and the lower portion of the grooved region [Figs. 5(b) and 5(c), case i]. As Re increases, the small scale features gain in energy and they become more visible in the plots of $(\boldsymbol{\phi}_3,\boldsymbol{\phi}_4)$ and $(\boldsymbol{\phi}_5,\boldsymbol{\phi}_6)$ at $\mathrm{Re}=750$ and $\mathrm{Re}=1050$ [see Figs. 5(b) and 5(c), cases ii and iii]. Note that the decrease in the relative contribution of the first modal pair to the total fluctuation energy budget does not significantly effect the appearance of the first and second eigenfunctions [Fig. 5(a), cases i–iii]. However, as Re increases, small scale features become bigger in size, stretch through the middle and groove portions of the channel, and gain in fluctuation intensity [see Figs. 5(b) and 5(c)].

The effect of Reynolds number on the temperature eigenfunctions is shown in Fig. 6. The large scale structures present in the first modal pair (ψ_1,ψ_2) shrink slightly as Re increases [Fig. 6(a)], while the second [Fig. 6(b)] and third [Fig. 6(c)] modal pairs gain energy and their characteristic closed isotherm structures become bigger in size. For $\mathrm{Re}=430$ and $\mathrm{Re}=750$, the small scale structures in (ψ_3,ψ_4) form three layer patterns in the bypass region of the channel.

TABLE III. Critical Reynolds number as predicted by various LOMs.

Model	Re at the onset of oscillations
LOM_{430}, $M_1=M_2=4$	320
LOM_{1050}, $M_1=M_2=4$	330
LOM_{1050}, $M_1=M_2=8$	350

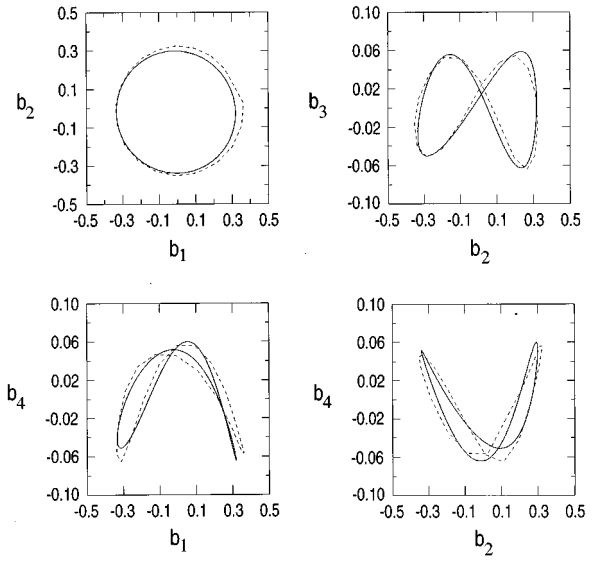

FIG. 10. Comparison of low-order model predictions with full-model results for $\mathrm{Re}\neq\mathrm{Re}_0$, and $\mathrm{Pr}=\mathrm{Pr}_0=0.71$. Solid line: ($\mathrm{LOM}_{430}$, $M_1=M_2=4$) predictions for $\mathrm{Re}=750$. Dotted line: Full model results for $\mathrm{Re}=750$.

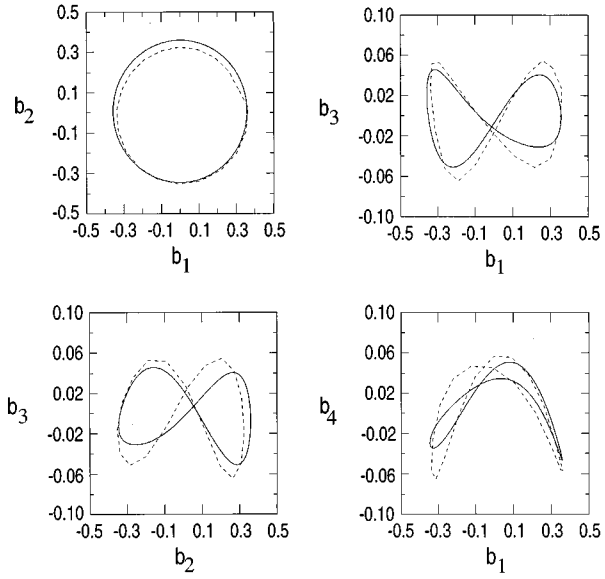

FIG. 12. Comparison of low-order model predictions with full-model results for $\mathrm{Re}\neq\mathrm{Re}_0$ and $\mathrm{Pr}=\mathrm{Pr}_0=0.71$. Solid line: ($\mathrm{LOM}_{1050}$, $M_1=M_2=4$) predictions for $\mathrm{Re}=750$. Dotted line: Full model results for $\mathrm{Re}=750$.

At $\mathrm{Re}=1050$, these structures have merged to form a two-layer pattern of larger and more energetic structures [Fig. 6(b)]. Thus, as Re increases, significant changes in the spatial characteristics of the temperature eigenfunctions are observed in accordance with the substantial redistribution of fluctuation energy among the six most energetic temperature eigenmodes.

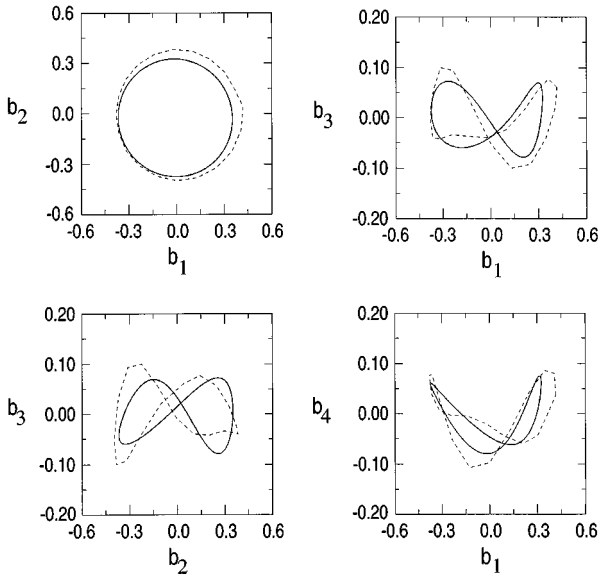

FIG. 11. Comparison of low-order model predictions with full-model results for $\mathrm{Re}\neq\mathrm{Re}_0$ and $\mathrm{Pr}=\mathrm{Pr}_0=0.71$. Solid line: ($\mathrm{LOM}_{430}$, $M_1=M_2=4$) predictions for $\mathrm{Re}=1050$. Dotted line: Full model results for $\mathrm{Re}=1050$.

C. Spatio-temporal structures

The temporal expansion coefficients, obtained by direct projection of the input velocity and temperature data on the computed eigenfunctions, are plotted in Fig. 7. Note that, as expected, the amplitudes of the temporal expansion coefficients increase as Re increases. The temporal expansion coefficients corresponding to a pair, i.e., (a_1,a_2), (a_3,a_4), (b_1,b_2), (b_3,b_4), etc., are phase shifted by a quarter of a period. We have seen in the previous section that the computed eigenfunctions (stationary spatial structures) also come in pairs with a phase shift of approximately a quarter wavelength in the bypass portion of the channel. Noting that the product $a_i\boldsymbol{\phi}_i$ (no summation) represents a standing wave and recalling that when two standing waves are out of phase by a quarter period both in time and space, a travelling wave is formed,[25] we may define for the problem at hand dynamical (spatio-temporal) coherent structures of velocity, $\boldsymbol{\xi}_m(\mathbf{X},t)$, and temperature, $\zeta_m(\mathbf{X},t)$, as follows:

$$\boldsymbol{\xi}_1(\mathbf{X},t)=\sum_{i=1}^{2} a_i(t)\boldsymbol{\phi}_i(\mathbf{X}),$$

$$\boldsymbol{\xi}_2(\mathbf{X},t)=\sum_{i=3}^{4} a_i(t)\boldsymbol{\phi}_i(\mathbf{X}),\ldots, \tag{12}$$

$$\zeta_1(\mathbf{X},t)=\sum_{i=1}^{2} b_i(t)\psi_i(\mathbf{X}),$$

$$\zeta_2(\mathbf{X},t)=\sum_{i=3}^{4} b_i(t)\psi_i(\mathbf{X}),\ldots, \tag{13}$$

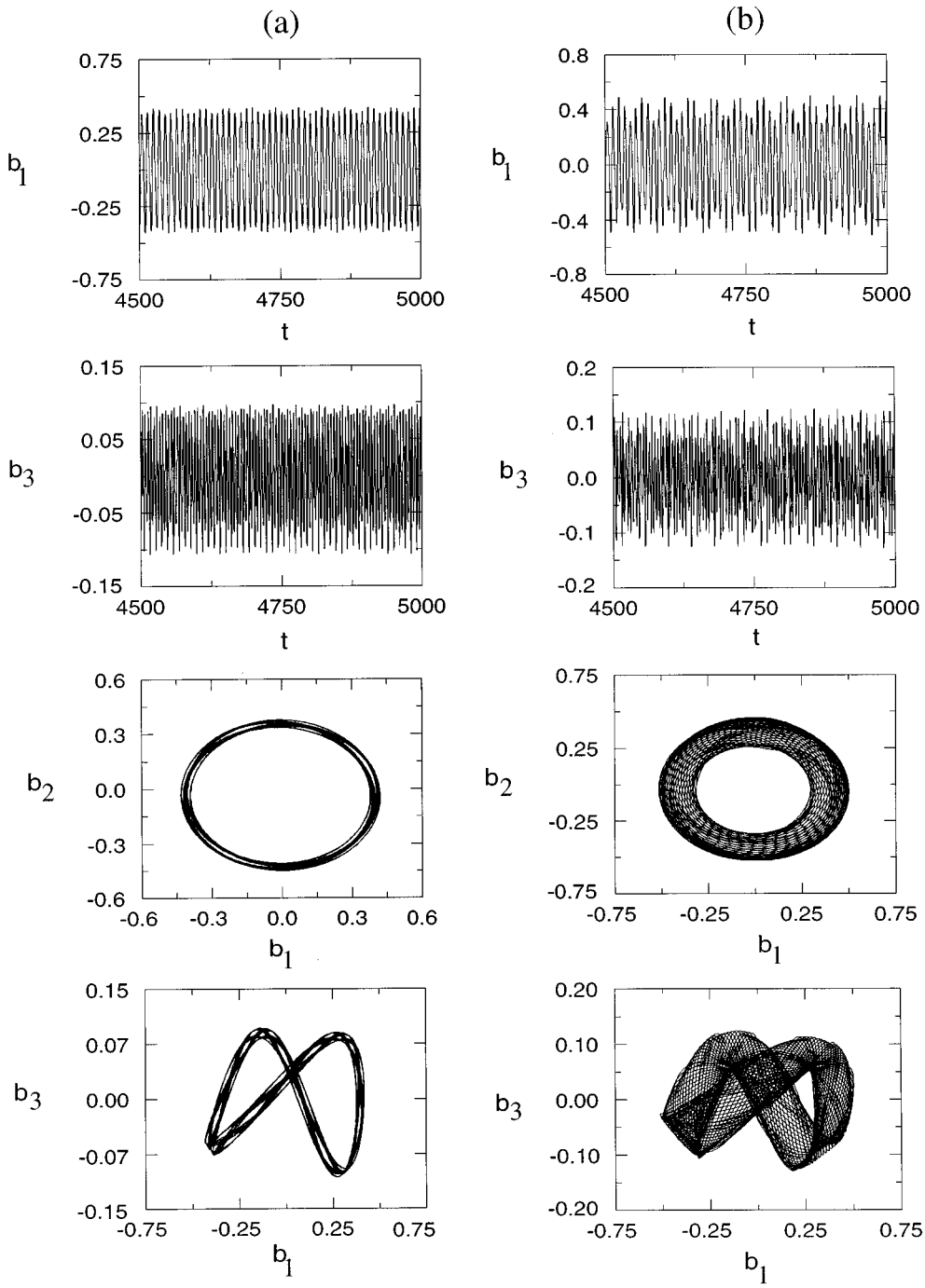

FIG. 13. Computed time series and phase space portraits of temperature expansion coefficients based on (LOM_{430}, $M_1=M_2=4$), $Pr=Pr_0=0.71$. (a) $Re=5000$, (b) $Re=5500$.

and identify them approximately as traveling waves. The evolution of $\zeta_1(\mathbf{X},t)$ and $\zeta_2(\mathbf{X},t)$ is shown in Fig. 8 for $Re=430$. Note that a pair of stationary eigenfunctions contain information on the typical shape of the corresponding dynamical (spatio-temporal) coherent structure since each eigenfunction can be considered as a coherent structure at a specific instant in time.

D. Low-order models

In developing a low-order model it is desired to keep as few modes as possible in the system of ordinary differential equations. However, enough modes need to be retained so that the field variables are reconstructed accurately, most of the flow and temperature fluctuation energy is captured, and the potentially important information hidden in the small scale features of higher modes is not lost. In practice, although the reconstruction error in Eq. (9) decreases as the number of retained modes increases, increasing the number of modes in the low-order model may not improve its performance due to the inevitable noise present in the computed high order eigenfunctions. Recall that, in contrast to the proper orthogonal decomposition and reconstruction proce-

dures, the Galerkin projection requires the computation of spatial derivatives of the eigenfunctions, a process that leads to noise amplification.

E. Low-order model predictions at "design" conditions

In applying the procedure described in Sec. III, the input time-dependent data are calculated at some values of the controling parameters $\mathrm{Re}=\mathrm{Re}_0$ and $\mathrm{Pr}=\mathrm{Pr}_0$. We refer to these parameters as design parameters or design conditions. In this paper, emphasis is given to airflow ($\mathrm{Pr}=\mathrm{Pr}_0=0.71$) at $\mathrm{Re}_0=430$, 750, and 1050. The case $\mathrm{Pr}=\mathrm{Pr}_0=7.1$ is briefly discussed in Sec. V. For each case, Eqs. (10) and (11) are integrated numerically using a fourth order Runge–Kutta solver. The temporal expansion coefficients calculated based on the three low-order models developed at $\mathrm{Re}_0=430$, 750, and 1050 with $M_1=M_2=4$ are shown in Fig. 9 after all transients have died out. These are limit cycle solutions as can be easily verified by plotting the orbits in the state space. These predictions are in very good agreement with the expansion coefficients obtained by direct projection of the full model data on the computed eigenfunctions shown in Fig. 7. Predictions based on the low-order models exhibit oscillations of correct frequency but of slightly larger amplitude than those calculated by direct projection. Similar results are obtained with a (6+6)-equation model.

F. Low-order model predictions for $\mathrm{Re}\neq\mathrm{Re}_0$

In the remainder of this section a notation of the form (LOM_{430}, $M_1=M_2=4$) refers to the low-order model constructed at design parameter $\mathrm{Re}_0=430$ keeping four terms in the velocity field expansion and four terms in the temperature field expansion [see Eq. (9)]. All results presented in this section describe temporal behavior after all initial transients die out.

Before discussing the predictions of the reduced models for $\mathrm{Re}\neq\mathrm{Re}_0$, let us summarize the basic characteristics of the flow under study. For small values of Reynolds number the flow is time independent. The flow becomes unstable (bifurcation to time-periodic solution) at $\mathrm{Re}\simeq 300$ and it exhibits self-sustained time-periodic oscillations for $300\leqslant\mathrm{Re}\leqslant 1050$.

Each of the LOMs reproduces successfully the dynamical behavior of the velocity and temperature fields for $\mathrm{Re}\leqslant 1050$ as long as $M_1>3$ and $M_2>3$. The conditions at the onset of spontaneous oscillations are predicted well by the LOMs. Table III lists the values of the critical Reynolds number as predicted by various LOMs.

In the range $430\leqslant\mathrm{Re}\leqslant 1050$ we have compared the LOM predictions with the corresponding full model solutions. In this range of Reynolds number, the LOMs predict self-sustained time-periodic behavior in agreement with the full model, as long as $M_1\geqslant 4$ and $M_2\geqslant 4$. The frequency of oscillations is predicted very accurately although the amplitude of oscillations is less accurately predicted by the LOMs (see Figs. 10–12).

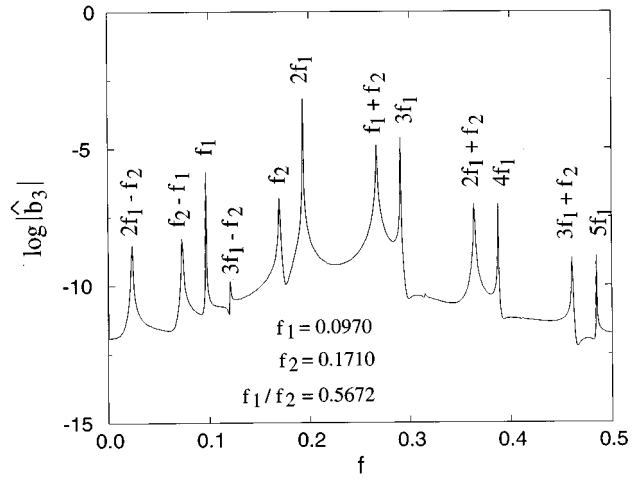

FIG. 14. Magnitude of Fourier transform of $b_3(t)$ at $\mathrm{Re}=5500$. (LOM_{430}, $M_1=M_2=4$), $\mathrm{Pr}=\mathrm{Pr}_0=0.71$.

For higher values of Re the solutions of LOMs undergo a series of bifurcations leading to chaotic behavior. Although the LOMs are not expected to be accurate far from the design conditions, we summarize here a few important characteristics of the model predictions for large Re. The models exhibit different routes to chaos depending on the number of modes retained (order of truncation). For example, Fig. 13 shows the long time predictions of (LOM_{430}, $M_1=M_2=4$) at $\mathrm{Re}=5000$ and $\mathrm{Re}=5500$ indicating transition to solutions of higher temporal complexity. The left column corresponds to the solution at $\mathrm{Re}=5000$ while the right column corresponds to $\mathrm{Re}=5500$. Figure 14 shows the magnitude of the Fourier transform, $\hat{b}_3(f)$, of $b_3(t)$ at $\mathrm{Re}=5500$. A period doubling bifurcation undergone by (LOM_{1050}, $M_1=M_2=6$) at $\mathrm{Re}\simeq 5000$ is shown in Figs. 15 and 16. Here the left column corresponds to the solution at $\mathrm{Re}=4500$ while the right column depicts the solution at $\mathrm{Re}=5000$. For a fixed truncation level, the predicted route to chaos is not altered by small changes in the initial conditions or small variations in the coefficients of Eqs. (10) and (11). These small variations may arise when different numerical integration and differentiation methods are used in implementing the approach described in Sec. III (e.g., spectral vs finite-difference based methods). Note that due to the forcing of the temperature field by the velocity field built in Eqs. (1)–(3) and (10) and (11), the temperature coefficients may exhibit quasiperiodic behavior while the velocity modes exhibit time-periodic (limit cycle) oscillations for some ranges of Re. This is the case, for example, for (LOM_{1050}, $M_1=M_2=4$) at $\mathrm{Re}\simeq 9500$ and (LOM_{1050}, $M_1=M_2=8$) at $\mathrm{Re}\simeq 14000$. Note also that for sufficiently large values of Reynolds number, the solutions of LOMs blow up. In general, inclusion of more modes in the model delays this behavior to higher values of Re.

The authors are not aware of any systematic investigation of the sequence of bifurcations leading to chaos in the open flow system under study. As mentioned before, no claim of quantitative agreement between the LOM predictions far from the design conditions and the full model solu-

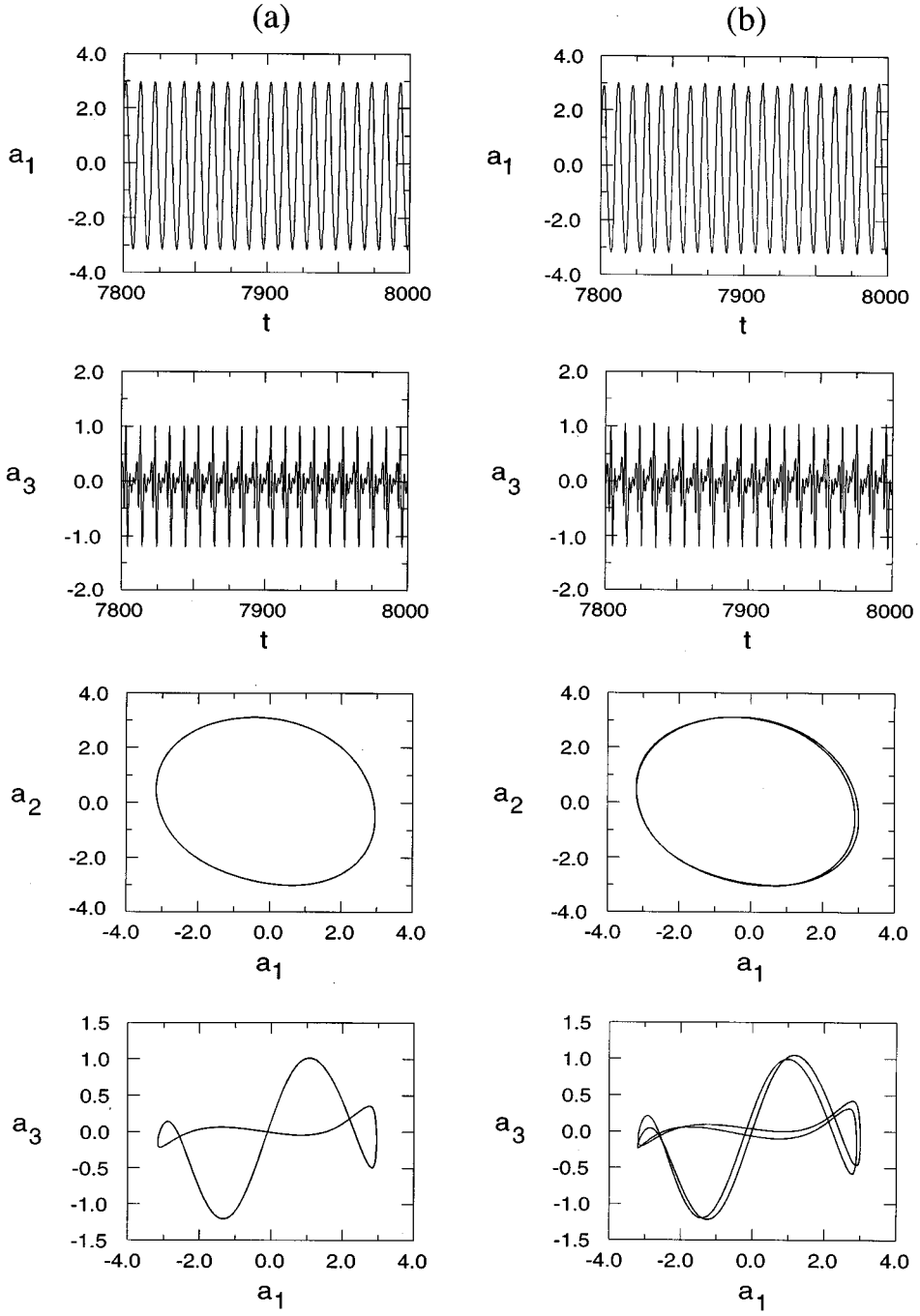

FIG. 15. Computed time series and phase space portraits of velocity expansion coefficients based on (LOM_{1050}, $M_1=M_2=6$), $Pr=Pr_0=0.71$. (a) $Re=4500$, (b) $Re=5000$.

tions is made here. However, the low-order models exhibit properties that are qualitatively in agreement with Navier–Stokes solutions for flows in other open systems (see, for example, the quasiperiodic solutions reported by Guzman and Amon[26] for a converging-diverging channel with smooth walls).

V. RESULTS FOR Pr=7.1

The method described in the previous sections was applied to spectral element solutions of Eqs. (1)–(3) computed for $Pr_0=7.1$ and $Re_0 = 430$. The flow field and consequently the velocity eigenfunctions are unaffected by the change in the value of Prandtl number due to the one way coupling of the governing equations. Figure 17 shows the computed temperature eigenfunctions. The eigenfunctions come in pairs, with a quarter-wavelength phase shift within each pair. This is consistent with the traveling wave nature of the disturbances discussed in Sec. IV C. The character of the first pair (ψ_1, ψ_2) is basically unaffected by the change in Pr [compare Fig. 17 with Fig. 6(a), case i]. However, the second pair (ψ_3,

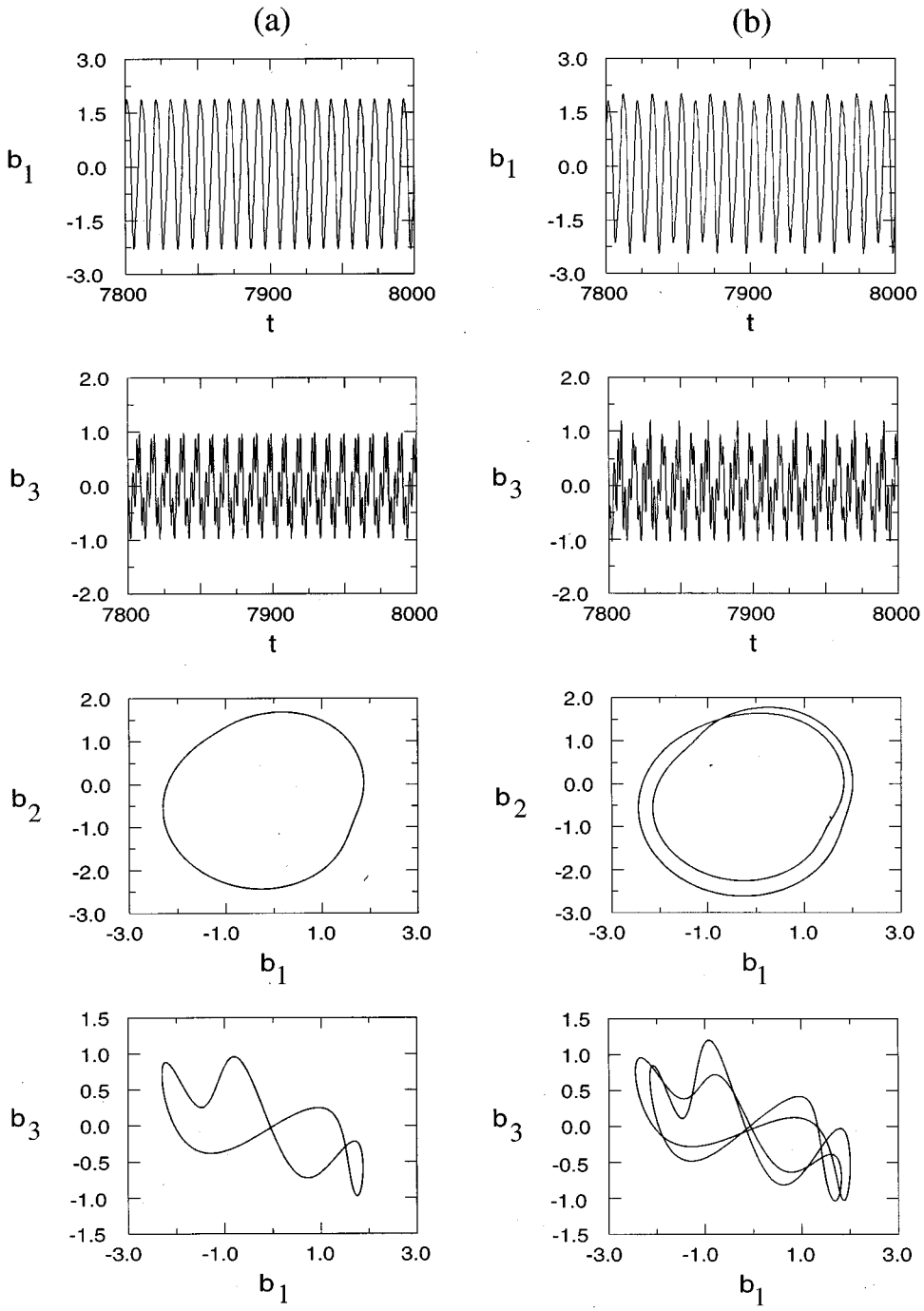

FIG. 16. Computed time series and phase space portraits of temperature expansion coefficients based on (LOM_{1050}, $M_1=M_2=6$), $Pr=Pr_0=0.71$. (a) $Re=4500$, (b) $Re=5000$.

ψ_4) captures smaller scale features than the corresponding eigenfunctions for $Pr=0.71$ [compare Fig. 17 with Fig. 6(b), case i]. Note also that (ψ_3, ψ_4) for $Pr=7.1$ are ''noisier'' than (ψ_3, ψ_4) for $Pr=0.71$. The low-dimensional model derived for ($Re_0=430$, $Pr_0=7.1$, $M_1=M_2=4$) reproduces successfully the dynamical behavior of the temperature field at design conditions (see Fig. 18). Far from the design conditions, as Re is increased, changes in the character of the temperature coefficients, $b_i(t), i=1,2,...,4$, are qualitatively similar to the ones discussed for $Pr=0.71$. However, the transition to complex temporal behavior takes place much earlier, at values of Re as low as 3000.

VI. CONCLUSIONS

Transitional flow in a periodically grooved channel has been analyzed by the method of empirical eigenfunctions or

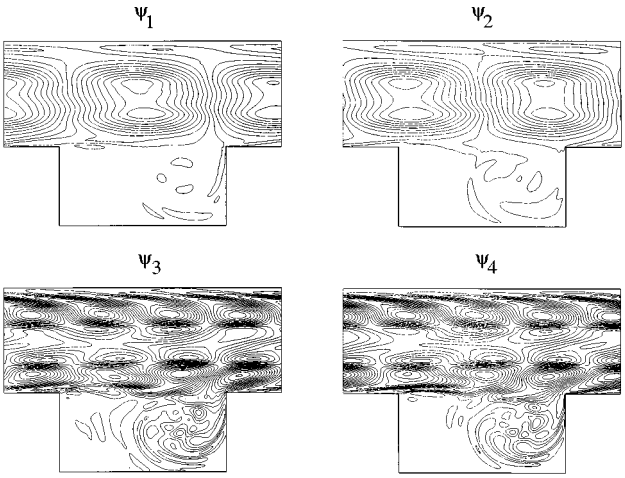

FIG. 17. Temperature empirical eigenfunctions (isotherms) at Re=430, Pr =7.1.

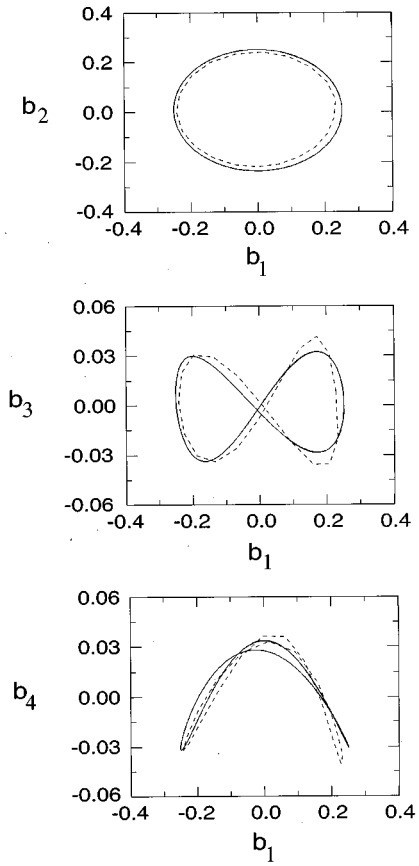

FIG. 18. Comparison of low-order model predictions with full-model results at design conditions. $Re_0=430$, $Pr_0=7.1$. Solid line: (LOM_{430}, $M_1=M_2=4$) predictions. Dotted line: Full model results.

proper orthogonal decomposition in order to extract the coherent structures of the flow and to develop realistic dynamical low-order models.

The dynamical (spatio-temporal) coherent structures are identified as traveling waves, formed by two standing waves that are out of phase by approximately a quarter period in time and space. For fixed Pr, the eigenvalues, eigenfunctions and coherent (spatio-temporal) structures depend on the Reynolds number. The dependence of the two most energetic eigenfunctions of each field [($\boldsymbol{\phi}_1$, $\boldsymbol{\phi}_2$) and (ψ_1, ψ_2)] on Reynolds number is weak. As Re increases, high order POD eigenfunctions gain energy and their relative contribution to the total fluctuation energy increases. Most of the transferred energy is gained by the third and fourth eigenmodes, and the remaining is distributed among the higher modes. The energy gain of higher modes affects the eigenfunctions, causing existing structures to stretch and become larger and new small scale structures to form. The extent of energy redistribution is higher for the temperature field than for the velocity field.

The accuracy of the constructed low-order models depends strongly on the number of modes retained. For the range of Re studied, at least four modes for velocity and four modes for temperature are required to predict self-sustained oscillations in time at design conditions. Retaining more than six modes may actually decrease the accuracy of the LOMs because high order POD eigenfunctions are, in general, less accurately calculated than the low-order most energetic ones. Close to the design conditions, the LOM predictions are in good agreement with the full model results. Far from the design conditions, the LOMs exhibit different routes to chaos depending on the order of truncation (number of modes retained). Ranges of Reynolds number for which quasiperiodic solutions and period-doubling bifurcations exist have been determined by numerically solving the ordinary differential equations.

Direct numerical simulations of transitional and turbulent thermofluid systems demand enormous computer resources. Galerkin projection using POD eigenfunctions leads to low-order models that accurately predict the systems' dynamical behavior in the vicinity of the design conditions, thus significantly reducing the computational effort in the analysis and simulation of these systems. We believe that low-order modeling has the potential of becoming a very useful tool in the study of coherent structure dynamics, and in exploring ideas in the context of intelligent flow control schemes.

ACKNOWLEDGMENT

This work was partially supported by NASA/LeRC under Contract No. NAG3-1632.

[1]N. Aubry, P. Holmes, J. L. Lumley, and E. Stone, ''The dynamics of coherent structures in the wall region of a turbulent boundary layer,'' J. Fluid Mech. **192**, 115 (1988).
[2]A. E. Deane and L. Sirovich, ''A computational study of Rayleigh–Benard convection. Part I. Rayleigh-number scaling,'' J. Fluid Mech. **222**, 231 (1991).
[3]A. E. Deane, I. G. Kevrekidis, G. E. Karniadakis, and S. A. Orszag, ''Low-dimensional models for complex geometry flows: Application to grooved channels and circular cylinders,'' Phys. Fluids A **3**, 2337 (1991).
[4]D. Rempfer and H. F. Fasel, ''Dynamics of three-dimensional coherent structures in a flat-plate boundary layer,'' J. Fluid Mech. **275**, 257 (1994).
[5]H. Gunes, R. A. Sahan, and A. Liakopoulos, ''Low-dimensional representation of buoyancy driven flow in a vertical channel with discrete heaters,'' in *Enhancing Natural Convection Cooling of Electronic Systems and*

Components, Proceedings of the 30th National Heat Transfer Conference, Vol. 1, edited by A. Ortega and S. P. Mulay (ASME, HTD-Vol. 303, New York, 1995), pp. 125–137.
[6]H. Gunes, A. Liakopoulos, and R. A. Sahan, ''Low-dimensional description of oscillatory thermal convection: The small Prandtl number limit,'' Theor. Comput. Fluid Dyn. (in press).
[7]R. A. Sahan, H. Gunes, and A. Liakopoulos, ''Low-order modeling of isothermal transitional grooved-channel flow,'' Technical Report, Department of Mechanical Engineering and Mechanics, Lehigh University, Bethlehem, PA (1994).
[8]R. A. Sahan, H. Gunes, and A. Liakopoulos, ''Low-dimensional models for coupled momentum and energy transport problems,'' in *Cooling and Thermal Design of Electronic Systems*, edited by C. H. Amon (ASME, HTD-Vol. 319/EEP-Vol. 15, New York, 1995), pp. 1–15.
[9]D. Gottlieb and S. A. Orszag, *Numerical Analysis of Spectral Methods* (Society for Industrial and Applied Mathematics, Philadelphia, 1977).
[10]A. Liakopoulos and C. C. Hsu, ''On a class of compressible laminar boundary-layer flows and the solution behavior near separation,'' J. Fluid Mech. **149**, 339 (1984).
[11]A. Liakopoulos, ''Computation of high speed turbulent boundary-layer flows using the k-ϵ turbulence model,'' Int. J. Numer. Methods Fluids **5**, 81 (1985).
[12]J. L. Lumley, ''The structure of inhomogeneous turbulent flow,'' in *Atmospheric Turbulence and Radio Wave Propagation*, edited by A. M. Yaglom and V. I. Tatarski (Nauka, Moscow, 1967), pp. 160–178.
[13]L. Sirovich, ''Turbulence and dynamics of coherent structures: I–III.,'' Q. Appl. Math. **45**, 561 (1987).
[14]M. N. Glauser and W. K. George, ''Orthogonal decomposition of the axisymmetric jet mixing layer including azimuthal dependence,'' in *Advances in Turbulence*, edited by G. Comte-Bellot and J. Mathieu (Springer, New York, 1987).
[15]L. J. Lu and C. R. Smith, ''Velocity profile reconstruction using orthogonal decomposition,'' Exp. Fluids **11**, 247 (1991).
[16]*Eddy Structure Identification in Free Turbulent Shear Flows*, edited by J. P. Bonnet and M. N. Glauser (Kluwer, Dordrecht, The Netherlands, 1993).
[17]L. Sirovich, ''Analysis of turbulent flows by means of the empirical eigenfunctions,'' Fluid Dyn. Res. **8**, 85 (1991).
[18]G. Berkooz, P. Holmes, and J. L. Lumley, ''The proper orthogonal decomposition in the analysis of turbulent flows,'' Annu. Rev. Fluid Mech. **25**, 539 (1993).
[19]C. H. Amon and A. T. Patera, ''Numerical calculation of stable three-dimensional tertiary states in grooved-channel flow,'' Phys. Fluids A **1**, 2005 (1989).
[20]G. E. Karniadakis, ''Spectral element simulation of laminar and turbulent flows in complex geometries,'' Appl. Numer. Math. **6**, 85 (1989).
[21]C. H. Amon and B. B. Mikic, ''Numerical prediction of convective heat transfer in self sustained oscillatory flows,'' J. Thermophys. Heat Transfer **4**, 239 (1990).
[22]J. S. Nigen and C. H. Amon, ''Forced convective cooling enhancement of electronic package configurations through self-sustained oscillatory flows,'' ASME-J. Electron. Packaging **115**, 356 (1993).
[23]A. T. Patera, ''A spectral element method for fluid dynamics: Laminar flow in a channel expansion,'' J. Comput. Phys. **54**, 468 (1984).
[24]Nekton Users Manual (Nektonics Inc., Release 2.9, 1994).
[25]H. Georgi, *The Physics of Waves* (Prentice-Hall, Englewood Cliffs, NJ, 1993), pp. 173–202.
[26]A. M. Guzman and C. H. Amon, ''Transition to chaos in converging-diverging channel flows: Ruelle–Takens–Newhouse scenario,'' Phys. Fluids A **6**, 1994 (1994).